Effects of High Pressure on the Luminescence Spectra of $Eu(SO_4)_2 \cdot NH_4$ Microcrystals: Anisotropically Induced Structural Distortions

Concepción Cascales,*,† Alicia de Andrés,† and Javier Sánchez-Benitez†,‡

Instituto de Ciencia de Materiales de Madrid, Consejo Superior de Investigaciones Científicas, C/Sor Juana Inés de la Cruz, 3, Cantoblanco, 28049 Madrid, Spain, and Centre for Science at Extreme Conditions, Erskine Williamson Building, The King's Building, The University of Edinburgh, Mayfield Road, Edinburgh EH9 3JZ, United Kingdom

Received: October 16, 2007; In Final Form: December 4, 2007

The possibilities of the use of Eu^{3+} in extracting information of the pressure effects on the nature of its crystal site in the $NH_4 \cdot Eu(SO_4)_2$ catalytic host are closely inspected through the study of emission spectra for applied pressures up to 87 kbar. The phenomenological crystal field analysis of these spectra reveals clear discontinuities, at ∼30 kbar, the sharper ones, and then at ∼70 kbar, in crystal field strength trends, which taken together with structure-based simulations of crystal field interactions indicate well-defined pressure-induced anisotropic distortions in Eu^{3+} local environments.

Introduction

The two series of trivalent rare earth R^{3+} ammonium double sulfates, monohydrated with stoichiometry $NH_4R(SO_4)_2 \cdot H_2O$ for the smaller R as Y and Ho, or anhydrous $R(SO_4)_2 \cdot NH_4$, for larger R^{3+} cations as Nd and Eu, are interesting catalytic systems tested in hydrogenation of olefins and nitroaromatics as well as in oxidation of organic sulfides.[1,2] These materials, which combine the advantages of the catalytic properties of R^{3+} centers and the solid phase, the mild conditions for reactions and the possibility of recycling and reusing, are well qualified for the development of environmentally benign methods. In oxidation reactions of organic sulfides the high selectivity found in competitive reactions is associated with the specific local environment of R^{3+} catalytic metallic centers.[2] Understanding these processes includes the study of the R^{3+} site features—the nature of the coordination sphere as controlled by electrostatic interactions and interligand steric contrains—in the corresponding structure. Fortunately, R^{3+} cations constitute very useful probes of crystal site environments in inorganic and organic systems.[3,4]

It is well-known that information on the nature of R^{3+} environments, in terms of symmetry and covalence of bonds to the ligands, can be derived from the crystal field analysis of the optical spectra of R^{3+} centers in their hosts. From this point of view, changes around R^{3+} involving variations in symmetry, interatomic distances, and covalence with neighboring ligands, as for those that result from the partial or total substitution for other R^{3+},[5−7] or by tuning temperature and pressure, are usually tested from the crystal field analysis of spectroscopic data derived from optical absorption, photoluminescence (including the fluorescence line narrowing technique, for glass materials), and inelastic neutron scattering experiments.

Focusing on the pressure effects that characterize the R^{3+} optical spectra,[8−16] and because Eu^{3+} is the obvious choice among all R^{3+}, this work presents a systematic evaluation of a number of pressure-dependent characteristics of local Eu^{3+} environments, i.e., the covalence, evolution of the spin−orbit interaction, and very especially the symmetry and distribution of the distances to the ligands in the stoichiometric $Eu(SO_4)_2 \cdot NH_4$ crystal, through the analysis of room-temperature photoluminescence spectra under different pressure conditions. The good resolution of the emission transitions, due to the ordered crystalline nature of $Eu(SO_4)_2 \cdot NH_4$, along with the sequence of observed energy levels corresponding to $^5D_0 \rightarrow {}^7F_J$ transitions up to $J = 4$, beyond the $^7F_2$ usually studied for Eu^{3+} glass materials,[13−15,17,18] are advantages for achieving accurate results in the current parametrization of Eu^{3+} crystal field interactions. Afterward, from the comparison with estimated crystal field parameters derived from crystallographic data by using the semiempirical Simple Overlap Model (SOM),[19] an assessment and discussion on the possible origin of distortions affecting the Eu^{3+} environment will be derived. The current approach to this knowledge can help to interpreting mechanisms in the bonding of Eu^{3+}, that is, the catalytic center in $Eu(SO_4)_2 \cdot NH_4$, to its ligands in the formation of the catalytic intermediate complexes.

Experimental Section

Synthesis of the Sample and Crystallographic Background. Colorless crystals of $Eu(SO_4)_2 \cdot NH_4$ were synthesized hydrothermally from a reaction mixture containing $Eu(NO_3)_3 \cdot 6H_2O$, propylamine and dimethyl sulfoxide, heated in a stainless steel reactor at 170 °C during two weeks under autogenous pressure.[1]

The crystal structure, established by single-crystal X-ray diffraction, is monoclinic, space group $P2_1/c$ (No. 14), with $a = 8.8605(8)$ Å, $b = 7.1183(7)$ Å, $c = 10.669(1)$ Å, $\beta = 91.324(2)°$, and $Z = 4$.[1] It can be conceived as constituted by sheets of composition $[Eu(SO_4)_2]^-_\infty$, Figure 1a, stacked parallel to the *bc* plane, Figure 1b, in which a honeycomb (6, 3) layer of EuO_9 edge sharing polyhedra is linked to two different kinds of isolated sulfate SO_4^{2-} tetrahedra. These sheets are bent along the *a* direction, as viewed in the Figure 1b. Inside the interblock

* Corresponding author. E-mail: ccascales@icmm.csic.es. Fax: 34 913720623.
† Consejo Superior de Investigaciones Científicas.
‡ The University of Edinburgh.

10.1021/jp710044p CCC: $40.75
Published on Web 01/29/2008

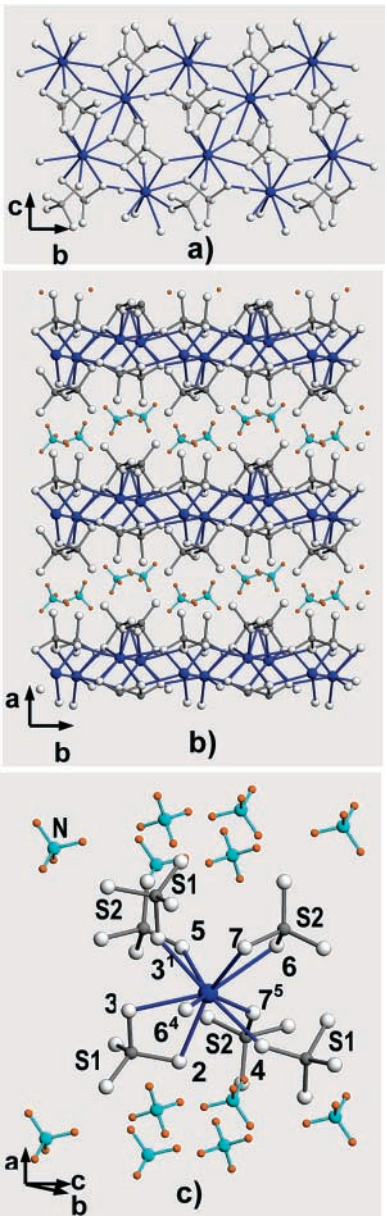

Figure 1. Views along (a) [100] and (b) [001] directions on the structure of $Eu(SO_4)_2 \cdot NH_4$. (c) Detailed view of the EuO_9 polyhedron and its environment. Large blue spheres represent Eu^{3+}, and labels for coordinated oxygens are those previously used in the single-crystal X-ray diffraction study);[1] SO_4^{2-} are the larger tetrahedral groups, and the smaller ones represent NH_4^+.

space are hosted rows of NH_4^+ running parallel to the *b* direction, connecting the layers through hydrogen bonds. The local structure around Eu^{3+} in the crystal, that is, its coordination polyhedron formed by oxygens as well as the nearest bonded SO_4^{2-} groups and NH_4^+ cations, is depicted in the Figure 1c.

Pressure Measurements and Photoluminescence Spectra. Pressure measurements were performed using a diamond anvil optical cell with steel gaskets with a typical 200 μm diameter hole. Single crystals of $Eu(SO_4)_2 \cdot NH_4$ were deposited on the top surface of a NaCl pellet inserted in the cell. This procedure avoids nonhydrostatic conditions during measurements, performed at pressures up to 87 kbar at room temperature. Ruby microspheres were also placed in the cell to measure the pressure by the ruby luminescence method.[20] In conjuction with the above cell, a micro-Raman system was used to obtain the Raman and emission spectra. The system consists in a Jobin-Yvon HR 460 monochromator, a N_2-cooled CCD and a Kaiser-Notch-Plus

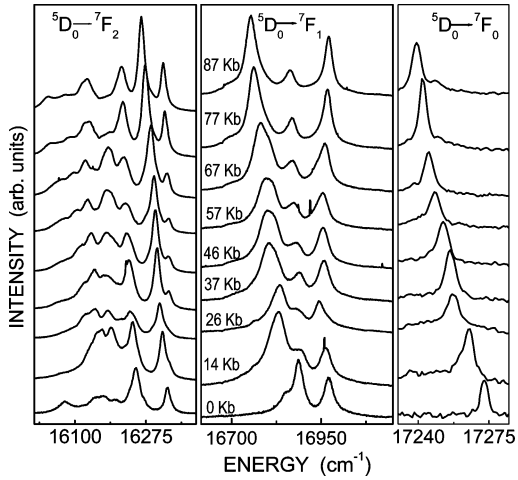

Figure 2. Room-temperature photoluminescence spectra for $^5D_0 \rightarrow {}^7F_{0,1,2}$ transitions of Eu^{3+} in $Eu(SO_4)_2 \cdot NH_4$ for measured pressures up to 87 kbar.

filter used to suppress the elastic scattered light. The 514.5 nm line of an Ar−Kr laser from Spectra Physics was used to excite the luminescence of the sample. The scattered and incident beams were focused using an Olympus microscope with a long working distance x20 objective; thus the experiments have been done in the backscattering geometry. At each pressure the scattered light from the sample and from one ruby sphere was collected.

Experimental Results

Depending on the applied pressure the collected luminescence spectra of $Eu(SO_4)_2 \cdot NH_4$, consisting of sharp and well defined $^5D_0 \rightarrow {}^7F_J$ transitions observed for $J = 0$, 1, 2, 3, and 4, present diverse characteristics, mainly regarding the individual positions of energy levels and therefore the magnitude of the observed crystal field splitting for each ^7F_J state, as well as their relative intensity. The evolution of energy level shifts shows strong nonlinearity between specific ranges of applied pressure. On the other hand, no induced amorphization has been observed,[21] and the small observed broadening for the single transition $^5D_0 \rightarrow {}^7F_0$ shows also nonlinear behavior with the compression. We shall hereafter refer to the optical features of these spectra—in terms of the position of the Stark energy levels, intensities of the corresponding transitions, and their line widths—as originating from Eu^{3+} at I, II, III, IV, V, VI, VII, VIII, and IX local environments, originated under pressures of 0, 14, 26, 37, 46, 57, 67, 77, and 87 kbar, respectively.

Figure 2 shows the spectra corresponding to the $^5D_0 \rightarrow {}^7F_{0,1,2}$ transitions at increasing pressures from ambient up to 87 kbar. In all cases, the observation of a weak line for the $^5D_0 \rightarrow {}^7F_0$ transition indicates a site of C_{nv}, C_n, or C_s symmetry for Eu^{3+}, as these symmetries allow the transition as an electric dipole process, according to the group theory selection rules, with a linear term in the crystal field expansion.[22,23]

Figure 3 summarizes the effects of pressure on the single $^5D_0 \rightarrow {}^7F_0$ transition. The energy of the transition for Eu^{3+} at I−IX environments is depicted in Figure 3a. Shifts to lower energies, from 17272 to 17239 cm^{-1}, are clearly observed when the pressure is getting higher. The red shift is very pronounced when the pressure was increased from ambient to 26 kbar, then the peak position remains practically unchanged between 26 and 37 kbar, showing a further moderate and continuous red shift above 37 kbar. In this way, two almost linear relationships, $^7F_0(A) = 17273 - 0.61P$ cm^{-1}, and $^7F_0(B) = 17267.8 - 0.34P$

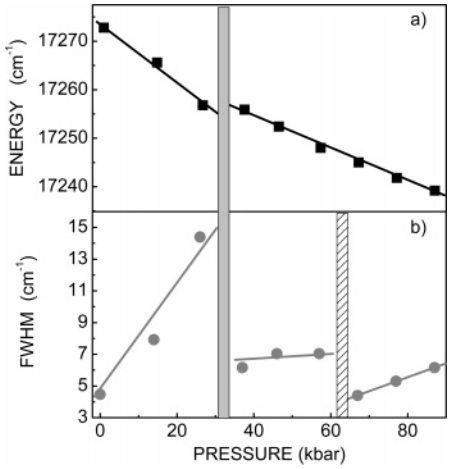

Figure 3. Energy (cm^{-1}) (a) and full width at half-maximum fwhm (b) of the $^5D_0 \rightarrow {}^7F_0$ transition of Eu^{3+} in $Eu(SO_4)_2 \cdot NH_4$ for measured pressures up to 87 kbar.

cm^{-1}, describe the dependence of the peak position with the pressure, with a clear change in the slope around 30 kbar, that separates the two main pressure-induced behavior regimes, A and B, as will be indicated below. Following previous arguments,[8,24] and according to the nephelauxetic effect,[25] we can evaluate the overall Eu−O bonding covalence for the different successive I−X sites by using the variation of the energy of the $^5D_0 \rightarrow {}^7F_0$ transition. Therefore, we associate the red-shifted transitions with increasingly covalent Eu^{3+} environments, this effect being strongly observed for I−III pressure-induced sites up to 26 kbar, and after the discontinuity around 30 kbar the increase in covalence becomes more gradual and continuous up to 87 kbar.

In the evolution of the bandwidth (as fwhm) of the $^5D_0 \rightarrow {}^7F_0$ transition, Figure 3b, an important broadening is initially observed, followed by a reversal in the trend around 30 kbar to more reduced fwhm values that remains nearly constant up to approximately 60 kbar. Finally, for the higher pressures the $^5D_0 \rightarrow {}^7F_0$ transition smoothly broadens again. This feature in $^5D_0 \rightarrow {}^7F_0$ can be ascribed to the correlation between electron−phonon coupling and crystal field strengths in a given pressure-induced Eu^{3+} environment.[26] These results, and the three pressure ranges that the evolution of the bandwidths establish, properly correlate with data obtained from the analysis carried out for selected Raman phonons of the $Eu(SO_4)_2 \cdot NH_4$ compound.[27] The maximum fwhm for site III at 26 kbar, about 3 times that for site I, suggests an increasing electron coupling to local lattice vibrations associated to an enhancement of the crystal field strength up to 26 kbar, which is followed by some weakening of these effects across IV−VII environments, and a final regain in them above 67 kbar, for Eu^{3+} at VIII and IX sites.

For all applied pressures, the presence of three Stark levels for the $^5D_0 \rightarrow {}^7F_1$ transition and five levels in the hypersensitive $^5D_0 \rightarrow {}^7F_2$ region, as Figure 2 shows, means that the degeneracy of these two states is completely lifted; that is, the crystal site of the Eu^{3+} optical center in I−IX surroundings possesses C_{2v} or lower symmetry. Table 1 includes the energies of the $^5D_0 \rightarrow {}^7F_0$ transition, $^7F_1$ and $^7F_2$ Stark levels, splittings, and centers of gravity for $^7F_1$ and $^7F_2$ states for Eu^{3+} in all I−IX environments.

The pressure is expected to increase the overlap between Eu^{3+} 4f wavefunctions and the ligand orbitals, yielding small variations on the Coulomb and spin−orbit coupling interactions. From the centers of gravity for $^7F_2$ and $^7F_1$ manifolds, an indication of the evolution of the spin−orbit coupling parameter ξ_{4f} with the pressure can be extracted.[8] Figure 4 gives the evolution with the compression of the average value ξ_{4f}. Initially, no variation is found, and the strong decrease of ξ_{4f} up to 37 kbar is followed by a plateau that extends to about 67 kbar, which turns even to increase at pressures above 67 kbar. Although the ξ_{4f} evolution for Eu^{3+} across I−IV pressure-induced sites has been explained as the result of the expansion of the 4f wavefunctions of Eu^{3+},[8] a consequence of the screening of the nuclear charge by the increasingly overlap with orbitals from the ligands, the behavior above 37 kbar, with a minimum at 67 kbar (for site VII), would be the result of some axially induced stress effect, owing the sensitivity of ξ_{4f} to nonisotropic stresses,[28] although other effects[8] could simultaneously influence the ξ_{4f} variation with the applied pressure.

By checking the variation of the intensity ratio of the induced electric dipole ED $^5D_0 \rightarrow {}^7F_2$ to the magnetic dipole MD $^5D_0 \rightarrow {}^7F_1$ emissions, $I_{ED/MD}(1)$, Figure 5, related to the Judd−Ofelt parameter Ω_2,[29] an assessment of the evolution of short-range effects such as the distortion and covalence degree of the Eu^{3+} site,[3,9,13−15,29,30] can be derived. Although this relationship is ∼2 for ambient pressure, it reaches a maximum value of ∼2.5 for 46 kbar. These data indicate an enhancement of the electric dipole $^5D_0 \rightarrow {}^7F_2$ transition, which reveals increasing distortion and/or higher covalence in bonds to ligands surrounding Eu^{3+} in I−V pressure-induced sites. However, the variation of $I_{ED/MD}(1)$ does not display an unique trend along the series of emission spectra, and after reaching the maximum at 46 kbar, its behavior reverses to lower values, indicating some release of one or both indicated factors, and finally regains strength for the environment IX, corresponding to the highest applied pressure. The identification of the key factor to cause discontinuities will be discussed later, in connection with results of the crystal field analysis.

Among the remaining observed $^5D_0 \rightarrow {}^7F_{3,4}$ transitions shown in Figure 6, the $^5D_0 \rightarrow {}^7F_3$ transitions are detected with remarkable low intensity. In fact, these transitions are forbidden in first order by the ED and MD selection rules, and can be observed only as a consequence of the *J*-mixing, which mixes the $^7F_3$ wavefunctions with other ^7F_J ones, through the second- and fourth-order crystal field parameters. Lists with all observed energy levels for Eu^{3+} at corresponding I−IX surroundings for applied pressures are available in the Supporting Information.[31]

The variation of long-range effects around Eu^{3+}, that is, those related to the bulk properties of our material and to the Judd−Ofelt parameter Ω_4,[29] can be followed through the intensity ratio $I_{ED/MD}(2)$ of ED $^5D_0 \rightarrow {}^7F_4$ to MD $^5D_0 \rightarrow {}^7F_1$ emissions; see Table 1. $I_{ED/MD}(2)$ experiences significant but scattered changes for increasing pressures, from ∼1 for ambient pressure up to ∼10 for 46 kbar and 87 kbar. At this point it is worth noting that the transition $^5D_0 \rightarrow {}^7F_4$ develops a peculiarly high intensity for pressures above 14 kbar, being even stronger than the $^5D_0 \rightarrow {}^7F_2$ transition. This phenomenon can be interpreted in terms of the behavior of the Judd-Ofelt intensity parameters Ω_λ related to their dependence on the nature and local symmetry around Eu^{3+}, in such a way that a particular combination of enhancement for Ω_4 upon Ω_2, as derived from a long-range environment becoming more regular by the applied pressure, with the high polarizability of the chemical surroundings of Eu^{3+}, has to be taken into account to explain it.[32]

The crystal field analysis and simulation of Eu^{3+} experimental energy levels constitutes an easy and powerful tool to evaluate the pressure-induced changes in symmetry and distances around Eu in $Eu(SO_4)_2 \cdot NH_4$. The whole series of luminescence spectra

TABLE 1: Energy of the $^5D_0 \rightarrow {}^7F_0$ Emission (cm^{-1}), Energy Levels (cm^{-1}), Centers of Gravity CG (cm^{-1}), Splittings Δ (cm^{-1}) for $^7F_1$ and $^7F_2$ Multiplets, and Intensity Ratios of Transitions $^5D_0 \rightarrow {}^7F_2/{}^5D_0 \rightarrow {}^7F_1$, $I(1)$, and $^5D_0 \rightarrow {}^7F_4/{}^5D_0 \rightarrow {}^7F_1$, $I(2)$, for Pressure-Induced P (kbar) Eu^{3+} Environments E in $Eu(SO_4)_2 \cdot NH_4$

			$^7F_1$					$^7F_2$								
P	E	$^5D_0$	1	2	3	CG[a]	Δ^7F_1	1	2	3	4	5	CG[a]	Δ^7F_2	$I(1)$[b]	$I(2)$[c]
0	I	17272	302	387	422	370	120	944	1022	1072	1102	1197	1067	253	2.10	1.1
14	II	17265	302	379	434	372	132	949	1023	1076	1099	1198	1069	249	2.23	3.4
26	III	17257	313	379	422	371	109	947	1021	1076	1107		1038	160	2.27	1.9
37	IV	17256	298	368	451	372	153	924	953	1025	1078	1108	1018	184	2.45	3.8
46	V	17252	296	375	447	373	151	922	954	1024	1074	1112	1017	190	2.52	10.2
57	VI	17248	294	376	450	373	156	918	954	1025	1069	1117	1016	199	2.47	
67	VII	17245	284	376	463	374	179	917	958	1025	1069	1119	1016	202	2.42	
77	VIII	17242	275	374	481	377	206	920	968	1024	1106	1116	1027	196	2.37	4.1
87	IX	17239	268	375	485	376	217	921	976	1024	1108	1120	1030	199	2.38	9.8

[a] CG have been calculated as the average energy of the three $^7F_1$ and five $^7F_2$ Stark levels, respectively. [b] $I_{ED/MD}(1) = (^5D_0 \rightarrow {}^7F_2)/(^5D_0 \rightarrow {}^7F_1)$. [c] $I_{ED/MD}(2) = (^5D_0 \rightarrow {}^7F_4)/(^5D_0 \rightarrow {}^7F_1)$.

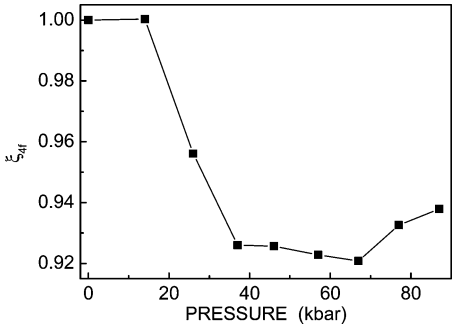

Figure 4. Effect of the applied pressure on the spin−orbit interaction ξ_{4f} normalized to the ξ_{4f} ($p = 0$ kbar) value.

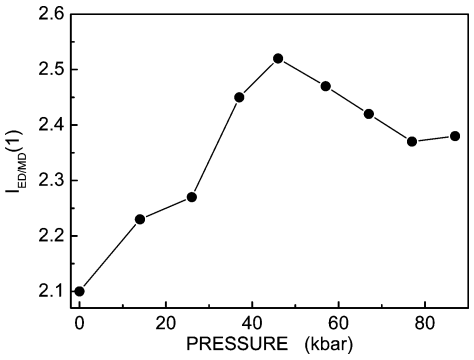

Figure 5. Intensity ratio $^5D_0 \rightarrow {}^7F_2/{}^5D_0 \rightarrow {}^7F_1$, $I_{ED/MD}(1)$, as a function of the applied pressure.

for I−IX environments will be examined to parametrize their corresponding crystal field interactions. The phenomenological evaluation of trends in derived crystal field parameters CFPs and their comparison with those derived from a semiempirical structure−related crystal field model, will provide a way to develop a description of the pressure relationship with local environments of Eu^{3+} active sites,[16] which must be consistent with all the results already pointed out.

Crystal-Field Analysis and Phenomenological Simulation of the Energy Level Schemes: Observed Trends. It is well-known that Eu^{3+} is the best choice for a "crystal-field probe" in a given host.[33] By making use of the selection rules for induced electric dipole and magnetic dipole transitions, it is possible to discriminate between different point symmetries for an observed optical center in a given host. Moreover, there is a straightforward relation between the crystal field splitting of $^{2S+1}L_J$ levels with small J values, especially for $J = 1$ and 2, and the CFPs. In this case, CFPs can be deduced directly from the experiment. The ^7F_J levels are very adequate to be used in a crystal field analysis because of their large value for the

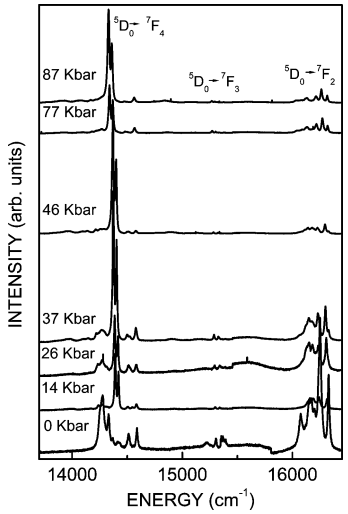

Figure 6. Room-temperature photoluminescence spectra for $^5D_0 \rightarrow {}^7F_{3,4}$ transitions of Eu^{3+} in $Eu(SO_4)_2 \cdot NH_4$ for measured pressures up to 87 kbar.

reduced matrix elements, and furthermore they can be described rather well in a Russell−Saunders basis,[34] in contrast with levels at higher energies.

The strongly reduced basis of the $^7F_{JM}$ set alone, i.e., 49 $\simeq |LJM_J\rangle$ levels, can be used to conduct, with accurate results, the phenomenological crystal field simulation of the Eu^{3+} energy level scheme.[3] Evidently, even with the J-mixing included, this basis does not take into account all interactions, as nondiagonal spin−orbit interactions that create small components of the ^5D_J levels into the ^7F_J wavefunctions. Therefore, "intermediate parameters" have to be introduced, one for each ^7F_J state, to overlap experimental and calculated centers of gravity.

The method used for calculating the energy levels of Eu^{3+} in a crystalline environment considers the single-particle crystal field theory. Following the formalism of Wybourne,[35] the crystal field Hamiltonian is expressed as a sum of products of tensor operators $(C_q^k)_i$, with real B_q^k and complex S_q^k parameters as coefficients, the latter appropriated to the Eu^{3+} site symmetry in the host.

$$H_{CF} = \sum_{k=2}^{4,6} \sum_{q=0}^{k} [B_q^k (C_q^k + (-1)^q C_{-q}^k) + iS_q^k (C_q^k - (-1)^q C_{-q}^k)]$$

The crystal field potential for Eu^{3+} in its initial environment in $Eu(SO_4)_2 \cdot NH_4$ possess C_1 symmetry[1] and thus involves 27 CFPs, but the simulation with such a high number of adjustable parameters is nonrealistic. Therefore, we proceeded by using

TABLE 2: Simple Overlap Model (SOM) Simulated, and Phenomenological Crystal Field Parameters and Crystal Field Strengths (cm^{-1}) for Eu^{3+} in Local Environments Induced by Pressure in $Eu(SO_4)_2 \cdot NH_4$

	SOM	I	II	III	IV	V	VI[c]	VII[c]	VIII	IX
B_0^2	*359*	306(8)	343(23)	332(17)	467(15)	468(16)	480(15)	518(12)	585(14)	609(14)
B_2^2	*228*	193(6)	174(18)	143(12)	146(14)	164(14)	172(15)	193(13)	223(14)	237(14)
B_0^4	*−518*	−905(12)	−888(34)	−951(25)	−375(28)	−405(29)	−426(30)	−401(23)	−237(27)	−214(30)
B_2^4	*−108*	−619(10)	−255(34)	−322(26)	−198(36)	−114(32)	−103(49)	−42(40)	−210(31)	−143(28)
B_4^4	*32*	−78(13)	−137(32)	−88(27)	−270(24)	−227(24)	−287(29)	−291(24)	−270(25)	−293(28)
S_2^4	*−568*	−320(18)	−697(29)	−761(17)	−530(20)	−546(25)	[−540]	[−540]	−504	−567(27)
S_4^4	*−107*	−156(13)	−22(38)	−150(24)	−239(26)	−267(27)	[−267]	[−267]	−296	−293(32)
B_0^6	*−51*	−354(16)	−259(46)	−363(43)	−299(30)	−256(31)	−380(30)	−309(30)	−466(32)	−505(34)
B_2^6	*−161*	−271(16)	−448(40)	−304(37)	−17(35)	−73(36)	−29(36)	−198(32)	−120(50)	−179(48)
B_4^6	*366*	361(14)	371(38)	410(21)	501(24)	515(23)	640(23)	639(22)	436(35)	513(29)
B_6^6	*6*	−296(16)	−336(53)	−735(23)	−718(39)	−828(32)	−756(34)	−713(32)	−953(27)	−1047(26)
S_2^6	*199*	314(14)	209(33)	174(20)	111(23)	68(26)	[70]	[70]	155(23)	204(24)
S_4^6	*−69*	−231(18)	−130(28)	−266(20)	−370(24)	−303(29)	[−332]	[−332]	−478(24)	−477(22)
S_6^6	*−122*	−285(15)	−622(45)	−486(34)	−710(27)	−711(33)	[−643]	[−643]	−433(32)	−139(68)
$S^{2\,a}$	*216*	183	189	174	228	234	241	262	297	311
S^4	*354*	454	463	504	340	339	349	343	329	345
S^6	*289*	301	379	430	475	495	493	486	506	527
S^T	*292*	332	362	396	362	372	376	375	388	406
N		21	20	18	22	22	11	11	18	18
σ^b		0.7	5.9	2.5	3.3	3.5	3.1	1.9	3.1	3.4

[a] $S^k = \{1/(2k+1)[(B_0^k)^2 + 2\sum_q[(B_q^k)^2 + (S_q^k)^2]]\}^{1/2}$, $S^T = [{}^1/_3\sum_k S^{k2}]^{1/2}$. [b] $\sigma = [\sum(\Delta_i)^2/(N-p)]^{1/2}$, $\Delta = E_o - E_c$; N = number of Stark levels, p = number of parameters. [c] Complex CFPs, with values close to those for V, have not been varied in the fit.

the approximate C_2/C_s symmetry, for all I−IX environments, as the best approach. To make a meaningful simulation, we carry out the descending symmetry procedure fitting first the observed energy levels in the orthorhombic C_{2v} point group, the highest symmetry for which no crystal field degeneracy exists. Thus, second-, fourth-, and sixth-rank real C_{2v} CFPs can be derived from the adequate reproduction of separate $^7F_1$,$^7F_2$ and the remaining observed $^7F_{3-4}$ splittings, respectively, before considering all observed energy levels and a free variation of all CFPs. This procedure often yields different sets of CFPs, all of them describing adequately the sequences of observed energy levels. This laborious procedure of searching reliable minima and accurate starting CFPs is facilitated by using predictive models for crystal field interactions,[36] that furthermore serve to assess the likeliness of present phenomenological parametrizations of crystal field effects in the Eu^{3+} initial I crystal site. We have applied the well-tested semiempirical Simple Overlap Model SOM.[19,37] This simplified model of calculation of crystal field interactions uses the crystal structural data concerning the closer coordination sphere of ions around Eu^{3+}, i.e., the distances in its coordination polyhedron.

SOM considers effective charges, located around the middle of the Eu^{3+}−ligand (L) distances, which are assumed to be proportional to the magnitude of the overlap integral ρ between the 4f and the valence orbitals of Eu^{3+} and L (oxygen), respectively. The CFPs are written as

$$B_q^k = \langle r^k \rangle \sum_L \rho_L \left(\frac{2}{1 \pm \rho_L}\right)^{k+1} A_q^k(L) \qquad \rho_L = \rho_0 \left(\frac{R_0}{R_L}\right)^{3.5}$$

The sum over L is limited to the first coordination sphere; consequently, the required crystallographic data are restricted to the closest oxygen positions and thus $\langle r^k \rangle$ radial integral are not corrected from the spatial expansion. ρ varies for each L as a function of the distance R, according to the exponential law above indicate, R_0 being the shortest distance. A_q^k is the lattice sum and it takes into account the symmetry properties of the Eu^{3+} site, including the effective charge attributed to L. The sign ± of the denominator stands for differentiating the type of L: when a single type of L is considered, a minus sign corresponding to the normal shift of the charge barycenter from the midpoint of the R bonding distance should be taken, and when different L are present the minus sign corresponds to the most covalent one. Crystallographic data for $Eu(SO_4)_2 \cdot NH_4$ were those from previous X-ray analysis,[1] the effective charge for the oxygen was taken as −1.0, a value that is found not to vary much, and ρ was adjusted to a value of 0.05, intermediate between typical values for $4f^N$ configurations, 0.04 (mostly ionic compounds) and 0.08 (mostly covalent compounds).[19] With this model, real B_q^k and complex S_q^k CFPs for the C_2/C_s symmetry of the initial environment I of Eu^{3+} in $Eu(SO_4)_2 \cdot NH_4$ have been estimated; see Table 2. These values together with the above phenomenological C_{2v} ones constitute the basis for subsequent C_2/C_s phenomenological fits of observed Eu^{3+} Stark energy levels.

To compare and evaluate changes in the crystal field interactions for Eu^{3+} in progressively pressure distorted local environments, the relative S^k ($k = 2, 4, 6$) and total S^T crystal field strength parameters have been also calculated; see definitions[38] at the bottom of Table 2. These S^2, S^4, and S^6 rotational invariants of the crystal field represent the short-, medium-, and long-range crystal field strengths, respectively, in connection to the spatial expansion of crystal field effects.

All the performed calculations were conducted with the aid of the matrix-diagonalizing program GROMINET,[39] which took into account the J mixing between wavefunctions with different J and M values. Least-squares refinements between experimental and calculated energy levels were carried out by minimizing the function σ, defined as indicated at the bottom of Table 2. Observed energy levels for Eu^{3+} at I−IX local fields, included in Table 1 of the Supporting Information, were used to determine the corresponding CFPs. These sequences include all well-resolved $^7F_1$ and $^7F_2$ Stark levels, which reduce possible uncertainties in calculated fourth rank CFPs, thus making their

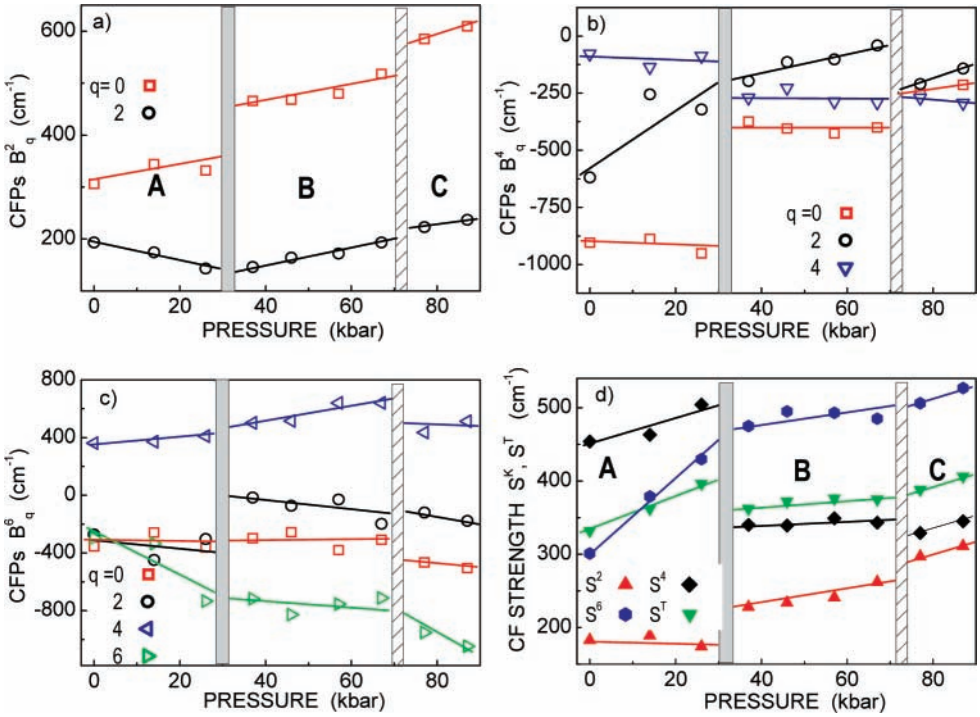

Figure 7. Variation of B^2_q (a), B^4_q (b), and B^6_q (c) crystal field parameters and crystal field strengths (d) as a function of the applied pressure for Eu^{3+} in $Eu(SO_4)_2 \cdot NH_4$.

values physically meaningful, and an important number of energy levels for $^7F_3$ and $^7F_4$ (excepting for 57 and 67 kbar measurements), which allows the fit of the sixth rank ones. In accordance with the reduced number of $^7F_3$ and $^7F_4$ observed energy levels in measurements at 57 and 67 kbar, complex four- and six-rank CFPs have not been varied in the fitting process, and their values were those obtained for the corresponding fit at 47 kbar. Final best fitted C_2/C_s CFPs for ambient and pressure-induced I−IX Eu^{3+} local environments in the studied ammonium sulfate matrix are listed in Table 2.

Despite the low point site symmetry of Eu^{3+} sites, the crystal field simulations have produced energy level sequences that show satisfying accordance with the observed data (see Table 2), and even more important, no individual discrepancies between experimental and calculated values of individual energy levels are observed. In the Supporting Information[31] are included the experimental sequences of energy levels and the corresponding calculated schemes for Eu^{3+} at I−IX environments.

Analysis of Trends in Phenomenological CFPs along the Pressure Series. To analyze possible trends with the applied pressure, results of Table 2 are displayed in Figure 7a−d. Apart from the nature of the considered R^{3+}, the crystal field potential around an optical center directly depends of the symmetry, distances, and bonding angles that characterize its crystallographic site in the host. If the applied pressure supposes some reduction in ligand distances around Eu^{3+}, yielding either higher symmetry sites or, in contrast, more distorted sites with wider distribution of distances (i.e., with some distance(s) significantly smaller than the average distance), the short-range crystal field strength would increase.

As shown in Figure 7a, an evolution to higher magnitudes can describe the general behavior of B^2_0 for I to IX Eu^{3+} surroundings, related to some reduction in nearer Eu^{3+}−ligand distances. However, a sudden jump in B^2_0 values is observed for pressures around 30 kbar, and after a continuous change to increased values, other less relevant discontinuity around 70 kbar up to 87 kbar is detected, delimiting three A, B, and C well-defined separate pressure-induced behaviors. Similar regions can be distinguished in the evolution of B^2_2 values, but for pressures below 30 kbar the evolution trend is reversed with regard to B^2_0. The crystal field strength parameter S^2, Figure 7d, which is a quantitative measure of the short-range crystal field interactions, smoothes to some extent the above opposite effects and, although it maintains the three differentiated pressure behavior ranges, evolves in a slightly increasing way across the series.

Concerning medium-range B^4_q CFPs, Figure 7b, the B^4_0 parameter undergoes an abrupt reduction of absolute values around 30 kbar, remaining afterward almost unchanged up to ∼70 kbar, and followed by a small increase for final pressures up to 87 kbar. Variations in the B^4_2 parameter, always with negative values, are weaker, but its trend delimits similar pressure ranges, with minima around 30 and 70 kbar. B^4_4 evolves depicting also the three indicated pressure schemes, with values going in the opposite direction with regard to B^4_0. Taking into account all these individual behaviors, the S^4 plot, Figure 7d, defines well the three kinds of behavior for medium-range Eu^{3+} crystal field interactions, and their corresponding pressure ranges, especially for the two first ones. Opposite trends of B^4_q CFPs featuring VIII and IX Eu^{3+} environments, for 77 and 87 kbar, respectively, cancel their differences with regard to IV−VII pressure-induced sites.

Being aware of the reduced number of experimentally observed $^7F_3$ and $^7F_4$ energy levels, and thus of the lower level of confidence, among B^6_q CFPs, Figure 7c, B^6_0 behaves fluctuant, with negative values and with a slightly negative slope from the start to the end of the series. For the B^6_2 parameter, also with negative values, after 30 kbar the pressure-induced Eu^{3+} environments show a reduction of its absolute value. The evolution of the B^6_4 parameter, with positive values in the whole pressure range, shows a positive slope up to ∼70 kbar, with somewhat lower values for the two environments corresponding to the higher pressures. Finally, the B^6_6 parameter

proceeds with a general increase of their negative values, with little variation in the pressure range between 30 and 70 kbar, with higher negative values for higher-pressure Eu^{3+} environments. The general behavior of S[6], Figure 7d, indicates a general enhancement of the strength in long-range crystal field interactions.

Locally Induced Pressure Effects around the Eu^{3+} Site: Discussion. Benefiting from the fact that the SOM model uses the crystallographic distances of the coordination polyhedron around Eu^{3+} in the estimation of CFPs, a qualitative evaluation of possible distortions induced in the $Eu(SO_4)_2 \cdot NH_4$ network by the applied pressure, through the adequate reproduction of the previously indicated trends in phenomenological CFPs, was attempted. Although the SOM is only a coarse approach, it is an attractive semiempirical crystal field model because of its simplicity correlating the crystal structure with CFPs. In SOM calculations only the first coordination sphere of neighbors around Eu^{3+}, i.e., the EuO_9 polyhedron (maximum distance $Eu-O_{max} = 2.580$ Å), is considered, but under the applied pressure it would be possible that some other ligands can be at similar distances from Eu^{3+} than those in EuO_9, contributing also to the crystal field felt by Eu^{3+}. Therefore, to extend our computations to a range of interatomic distances covering all possible ligands with effect over the Eu^{3+} crystal field, a modified model, SOMPLUS,[40] which also takes into account more distant ligands, S(1) and S(2) from SO_4^{2-} groups, NH_4^+, and even next Eu^{3+} in a second cationic sphere, has been used here. Bearing in mind the anisotropy of the studied material, these calculations have explored, together with the effect of the hydrostatic compression (H) on the $Eu(SO_4)_2 \cdot NH_4$ crystal, the pressure effect on each single crystallographic direction, that is, the calculation of CFPs supposing volume compressions derived from the reduction of unit cell dimensions along *a*, *b*, or *c* crystal axes (thereafter shortly indicated as *a*, *b*, or *c* volume compressions).

Because phenomenological fits have yielded remarkable variations and well-defined trends in the evolution with the pressure for B_0^k ($k = 2, 4, 6$) parameters, and especially for B_0^2 and B_0^4, the comparison with predictions derived from SOM and SOMPLUS will be focused on these CFPs. Figure 8a−c collects calculated B_0^k values vs volume compressions of the unit cell of $Eu(SO_4)_2 \cdot NH_4$, corresponding to Eu^{3+} surrounded by (i) oxygens of EuO_9 and (ii) ligands at larger distances, the above ones plus S(1) and S(2) from sulfate groups, NH_4^+ and a second sphere of Eu^{3+} cations, up to 7 Å. Due to the $1/R^{k+1}$ dependence, the consideration of environments including successive shells of ligands at a greater distance is supposed not much influence the crystal field. As can be seen in Figure 8a−c, no important differences have been found between (i) and (ii) surroundings for either B_0^4 or B_0^6 parameters, in any crystal direction, even at the highest considered pressure. Divergences are larger for B_0^2 ($1/R^3$ decreases slower than $1/R^5$ and $1/R^7$), with higher values for the extended environment of ligands. Therefore, the non-nearest neighbor ligands have a greater contribution to the parameters with $k = 2$, than those with $k = 4$ and 6. Moreover, these calculations indicate that the evolution of the crystal field interactions in $Eu(SO_4)_2 \cdot NH_4$ is highly anisotropic, and only the effect of the compression along *c* is close to the effect of the hydrostatic compression. Thus, sudden changes in phenomenological CFPs as those observed mainly around 30 kbar could be attributed to an emerging dominant axial component of the pressure-induced volume compression of the unit cell of $Eu(SO_4)_2 \cdot NH_4$.[8,11,28,41,42] In other words, changes in the main axial component of the nonhydrostatic

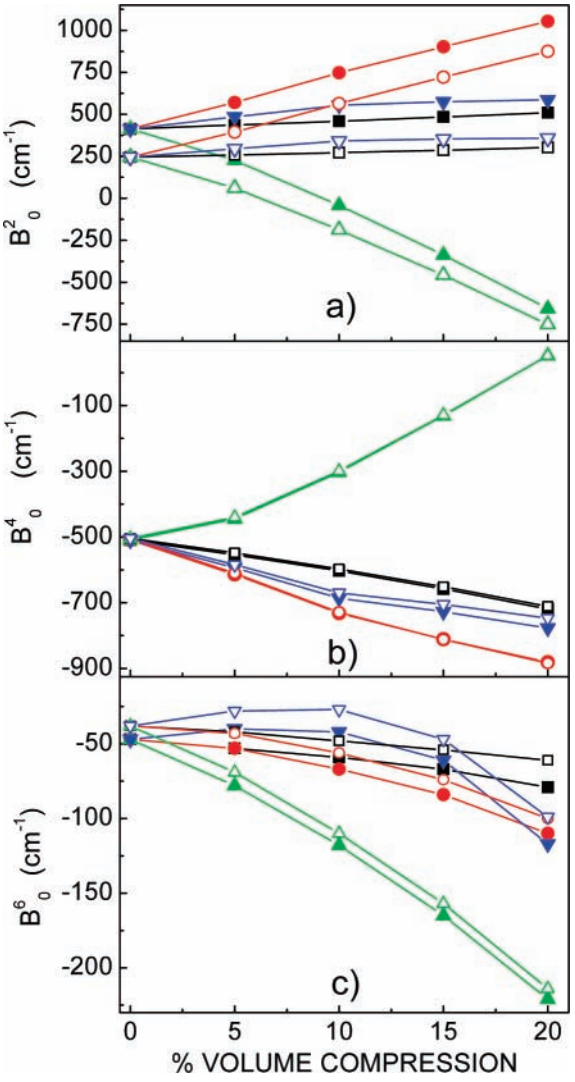

Figure 8. Variation of simulated (a) B_0^2, (b) B_0^4, and (c) B_0^6 Eu^{3+} crystal field parameters vs hydrostatic H (■), *a* (●), *b* (▲) and *c* (▼) volume compressions of $Eu(SO_4)_2 \cdot NH_4$. Open symbols are for calculations considering only the first shell of oxygens around Eu^{3+}, and full symbols are for ligands up to 7 Å from Eu^{3+}.

induced compression at a given pressure can account for important modifications of trends in CFPs.

Independently of the considered nearer or extended ligand field around Eu^{3+}, from the comparison of the phenomenological B_0^2 vs pressure, Figure 7a, with the calculated curves, Figure 8a, it can be derived that if initially the pressure effect on the crystal field can be assimilated to this produced by a hydrostatic regime, the sudden jump in B_0^2 must be attributed to a short-range compression experienced mainly along the *a*-axis. This means that for pressures exceeding a given limit the compression specifically affects ligands situated near the *a*-axis, those labeled O2, O4, O3[1], and O5 in Figure 1c, whose individual distances to Eu^{3+} are clearly diminished with regard to the average Eu−O(P), yielding a larger distribution of distances around Eu^{3+}, and thus stronger B_0^2 CFPs.[43]

The evolution of calculated B_0^4, Figure 8b, has negative slope for hydrostatic H as well as for both *a* and *c* volume compressions. On the contrary, it shows positive slope, going from strong negative to small positive values, for compressions induced along the *b*-axis. Thus, trends in phenomenological B_0^4 values could be reproduced through a change in the effect of the pressure, which specifically influences medium-range

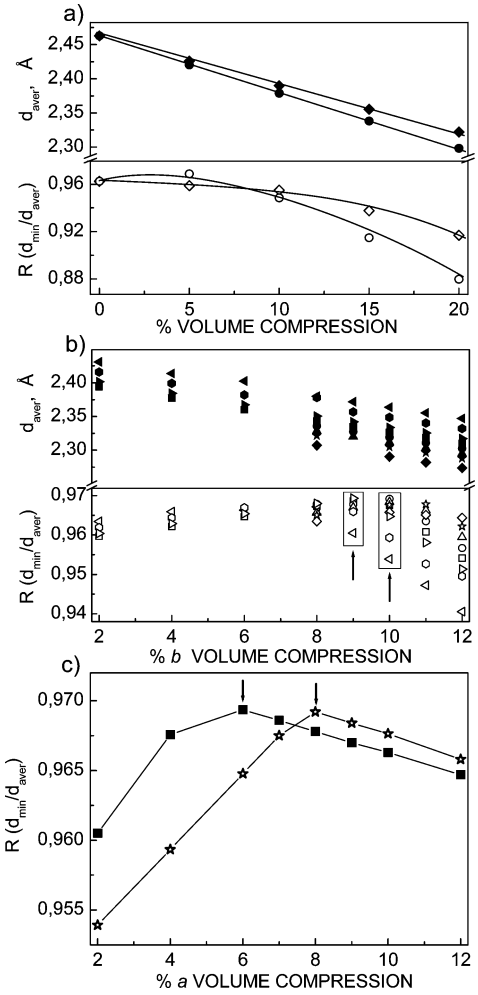

Figure 9. (a) Evolution of average Eu−O distances d_{aver} (full symbols) and R ratio (open symbols) in the EuO_9 polyhedron for independent a and b volume compressions: (◆) a volume compression; (●) b volume compression. (b) Evolution of d_{aver} (full symbols) and R ratio (open symbols) for mixed b and (left pointing triangle) 2%; (⬢) 4%; (right pointing triangle) 6%; (■) 7%; (●) 8%; (▲) 9%; (∗) 10%; (◆) 12% a volume compressions. (c) Evolution of R ratio for mixed a and (■) 9% and (∗) 10% b volume compressions.

distances around Eu^{3+} and supposes compression along the b direction. Above 30 kbar these effects at medium-range distances will result in a rather more regular environment of ligands around Eu, leading to weaker B_0^4 CFPs.

To better visualize the correlation between pressure effects with changes in the distribution of distances around Eu^{3+}, we have carried out the analysis of the evolution of all EuO_9 distances. Initially, the calculations have been made for a and b volume compressions, each one independently considered, and the results are collected in Figure 9a. It can be observed that both individual a and b compressions lead to lower Eu−O average distances, d_{aver}. However, the corresponding ratio between the minimum and the average values of Eu−O distances, $R = d_{min}/d_{aver}$, chosen as a figure of merit for the degree of regularity of the EuO_9 polyhedron, behaves differently. Though R values are nearly constant up to the 10% of a volume compressions, and then they diminish, a maximum is observed at ∼5% of b volume compression, and then its lessening is even more accentuated than for compressions along a. Afterward, the mixed effect of a and b volume compressions on Eu−O distances was scanned in the 2−12% region, and the results are collected in Figure 9b,c. Because R maxima have been detected in Figure 9b for 9 and 10% b volume compressions, both sets of data, for different a volume compressions, are displayed in Figure 9c. The two sets of combined a and b volume compressions yielding most regular EuO_9 environments, that is, R maxima, correspond to 6% a−9% b and 8% a−10% b effects.

Obviously, the evolution of B_0^2 toward higher values will be modulated and kept within narrower limits, mainly in the 37−60 kbar range of applied pressure, by this now homogenized distribution of distances around Eu^{3+}.

The phenomenological variation of B_0^6 with the pressure is not very well defined, and then its explanation is not as clear as that previously indicated for B_0^2 and B_0^4. In any case, because expected B_0^6 are going to increased negative values for purely hydrostatic as well as for volume compressions along the a and b directions, only the effect of the compression along c would account for the initial raise (up to ∼10% c volume) in observed B_0^6 values.

Conclusions

Although from ambient up to below ∼30 kbar the expected effects of the hydrostatic applied pressure are manifested through gradual changes in emission spectra, which involve the enhancement of the covalence and distortion of Eu−O bonds, the increasing strength of the electron−phonon coupling, the rapid decrease of the spin−orbit coupling related to the screening of nuclear charges and to the expansion of the 4f wavefunctions, along with some increase in the crystal field strengths, clear discontinuities appear around 30 kbar. Thus, a strong decrease in the electron−phonon coupling and the stabilization of the average value the spin−orbit interaction as well as sharp changes to higher B_0^2 (and S^2) and to lower B_0^4 (and S^4) values are the main characteristic for Eu^{3+} environment in this pressure range. The origin of this behavior can be attributed to anisotropic compressions induced in the network by the applied pressure. Through data derived from phenomenological crystal field analyses and structure-based crystal field simulations, it can be described as the result of (1) a short-range distortion felt along the a-axis, which specifically minimizes distances to ligands aligned along a, enlarging the distribution of Eu−O distances with regard to $Eu-O_{aver}$, and therefore yields enhanced B_0^2 values, and (2) a compression along b, which specifically influences medium-range distances around Eu^{3+}, generating more regular Eu^{3+} environments, and consequently lessens B_0^4 values. Reinforced trends to higher B_0^2 and lower B_0^4 CFPs for Eu^{3+} at VIII and IX environments resulting from applied pressures of 67−87 kbar can be understood not only by the strengthening of these anisotropies but also as related to the observed increase in the spin−orbit coupling, in which several effects, such as the increasing gradient with the distance of the effective potential or the increasing hybridization of 4f, 2s, and 2p orbitals, can be involved.[8]

An increase in the coordination number of ligands around Eu^{3+} in $Eu(SO_4)_2 \cdot NH_4$ with the applied pressure[9] has been discarded because of results from simulations of CFPs for sufficiently larger distances.

Furthermore, the careful analysis of the evolution of Eu−O distances resulting from possible anisotropically induced volume compressions even provides a semiquantitative relationship between crystal field effects in specific ranges of pressure with the local distortion of the network around Eu^{3+}.

The developed approach to the assessment of the nature of the environment of Eu^{3+} as based on the analysis of its photoluminescence spectra, can be also extended, in a more

general way, to the study of other systems, among which mono- and polymetallic molecular structures[4] or important biological systems[44] can be included.

Acknowledgment. We acknowledge the support from Spanish projects and MAT2004-2001, MAT2005-06354-C03-01, and MAT2006-01004.

Supporting Information Available: Tables with observed and calculated energy levels for observed pressure-induced local environments of Eu^{3+} in $Eu(SO_4)_2 \cdot NH_4$ (PDF). This information is available free of charge via the Internet at http://pubs.acs.org.

References and Notes

(1) Ruiz Valero, C.; Cascales, C.; Gómez Lor, B.; Gutiérrez Puebla, E.; Iglesias, M.; Monge, M. A.; Snejko, N. *J. Mater. Chem*. **2002**, *12*, 3073.

(2) Cascales, C.; Gómez Lor, B.; Gutiérrez Puebla, E.; Iglesias, M.; Monge, M. A.; Ruiz Valero, C.; Snejko, N. *Chem. Mater*. **2004**, *16*, 4144.

(3) Cascales, C.; Balda, R.; Fernández, J. *Opt. Express* **2005**, *13*, 2141.

(4) Bünzli, J. C. G.; Piguet, C. *Chem. Soc. Rev*. **2005**, *34*, 1048.

(5) Zaldo, C.; Rico M.; Cascales, C.; Pujol, M. C.; Massons, J.; Aguiló, M.; Díaz, F; Porcher, P. *J. Phys: Condens. Matter* **2000**, *12*, 8531.

(6) Cascales, C.; Zaldo, C.; Caldiño, U.; García Solé, J.; Luo, Z. D. *J. Phys: Condens. Matter* **2001**, *13*, 8071.

(7) Cascales, C.; Balda, R.; Fernández, J.; Fernández-Navarro, J. M. *J. Non-Cryst. Solids* **2006**, *352*, 2448.

(8) Huber, G.; Syassen, K.; Holzapfel, W. B. *Phys. Rev. B* **1977**, *15*, 5123.

(9) Lochhead, M. J.; Bray, K. L. *Phys. Rev. B* **1995**, *52*, 15763.

(10) Hua, H.; Vohra, Y. K. *Appl. Phys. Lett*. **1997**, *71*, 2602.

(11) Manjón, F. J.; Jandl, S.; Syassen, K.; Gesland, J. Y. *Phys. Rev. B* **2001**, *64*, 235108.

(12) Strässle, T.; Divis, M.; Rusz, J.; Janssen, S.; Juranyi, F.; Sadykov, R.; Furrer, A. *J. Phys.: Condens. Matter* **2003**, *15*, 3257.

(13) Reinsfeld, R.; Zigansky, E.; Gaft, M. *Mol. Phys*. **2004**, *102*, 1319.

(14) Jayasankar, C. K.; Ramanjaneya Setty, R.; Babu, P.; Tröster, T.; Holzapfel, W. B. *Phys. Rev. B* **2004**, *69*, 214108.

(15) Surendra, Babu, S.; Babu, P.; Jayasankar, C. K.; Tröster, T.; Sievers, W.; Wortmann, G. *J. Phys. Condes. Matter* **2006**, *18*, 1927.

(16) Troster, T. Optical studies of non-metallic compounds under pressure. In *Handbook on the Physics and Chemistry of Rare Earths*; Gschneidner, K. A., Jr., Bünzli, J.C-G., Pecharski, V. K., Eds.; Elsevier Science: Amsterdam, 2003; Vol. 33, p 51.

(17) Zambelli, M.; Abril, M.; Lavin, V.; Speghini, A.; Bettinelli, M. *J. Non-Cryst. Solids* **2004**, *345*, 386.

(18) Venkatramu, V.; Navarro-Urrios, D.; Babu, P.; Jayasankar, C. K.; Lavin, V. *J. Non-Cryst. Solids* **2005**, *351*, 929.

(19) Porcher, P.; Couto dos Santos, M.; Malta, O. *Phys. Chem. Chem. Phys*. **1999**, *1*, 397.

(20) Mao, H. K.; Xu, J.; Bell, P. M. *J. Geophys. Res*. **1986**, *91*, 4673.

(21) Hua, H.; Mirov, S.; Vohra, Y. K. *Phys. Rev. B* **1996**, *54*, 6200.

(22) Blasse, G.; Bril, A.; Nieuwpoort, W. C. *J. Phys. Chem. Solids* **1966**, *27*, 1587.

(23) Nieuwpoort, W. C.; Blasse, G. *Sol. State Commun*. **1966**, *4*, 227.

(24) Chen, G.; Haire, R. G.; Peterson, J. R. *J. Phys. Chem. Solids* **1995**, *56*, 1095.

(25) Jørgensen, C. K. *Prog. Inorg. Chem*. **1962**, *4*, 73.

(26) Avouris, P.; Campion, A.; El-Saled, M. A. *J. Chem. Phys*. **1977**, *67*, 3397.

(27) de Andrés, A.; Sanchez-Benitez, J.; Cascales, C.; Snejko, N.; Gutierrez Puebla E.; Monge, M. A. *Chem. Phys. Lett*. **2008**, *106*−*110*, 451.

(28) Adams, D. M.; Appleby, S. R.; Kharma, K. *J. Phys. E* **1976**, *9*, 5123.

(29) Oomen, E. W. J. L.; van Dongen, A. M. A. *J. Non-Cryst. Solids* **1989**, *111*, 205.

(30) Cascales, C.; Porcher, Fernández, P. J.; Oleaga, A.; Balda R.; Diéguez, E. *J. Alloys Compd*. **2001**, *323*−*324*, 260.

(31) See Supporting Information for lists with all observed and calculated energy levels for Eu^{3+} in $Eu(SO_4)_2 \cdot NH_4$, for each applied pressure and corresponding I−IX surroundings.

(32) Sá Ferreira, R. A.; Nobre, S. S.; Granadeiro, C. M.; Nogueira, H. I. S.; Carlos, L. D. and Malta, O. L. *J. Lumines.* **2006**, *121*, 561.

(33) Görller-Walrand C.; Binnemans, K. Rationalization of Crystal-Field Parametrization. In *Handbook on the Physics and Chemistry of Rare Earths*; Gschneidner, K. A., Jr., Eyring, L., Eds.; Elsevier Science: Amsterdam, 1996; Vol. 23, p 121.

(34) Ofelt, G. S. *J. Chem Phys*. **1963**, *38*, 2171.

(35) Wybourne, B. G. *Spectroscopic properties of Rare Earths*; Wiley: New York, 1965.

(36) Garcia, D.; Faucher, M. Crystal-field in non-metallic (rare-earth) compounds. In *Handbook on the Physics and Chemistry of Rare Earths*; Gschneidner, K. A., Jr., Eyring, L., Eds.; Elsevier Science: Amsterdam, 1995; Vol. 21, p 263.

(37) Cascales, C.; Zaldo, C.; Sáez, Puche, R. *Chem. Mater.* **2005**, *17*, 2052.

(38) Chang, N. C.; Gruber, J. B.; Leavitt, R. P.; Morrison, C. A. *J. Chem. Phys*. **1982**, *76*, 3877.

(39) Porcher, P. *Fortran routine* GROMINET *for simulation of real and complex crystal field parameters on* $4f^6$ *and* $4f^8$ *configurations*; 1995.

(40) Porcher P. *Fortran routine SOMPLUS for simulation of real and complex crystal field parameters on* $4f^n$ *configurations in materials with local disorder*; 2001.

(41) Hazen, R. M.; Finger, L. W.; Mariathasan, J. W. E. *J. Phys. Chem. Solids* **1985**, *46*, 253.

(42) Shen, Y.; Bray, K. L. *Phys. Rev. Lett*. **2000**, *84*, 3990.

(43) Haumesser, P. H.; Gaumé, R.; Viana, B.; Antic-Fidancev, E.; Vivien, D. *J. Phys. Condens. Matter* **2001**, *13*, 5427.

(44) See, for instance, Mundoma, C.; Greenbaum, N. L. *Biopolymers* **2003**, *69*, 100.